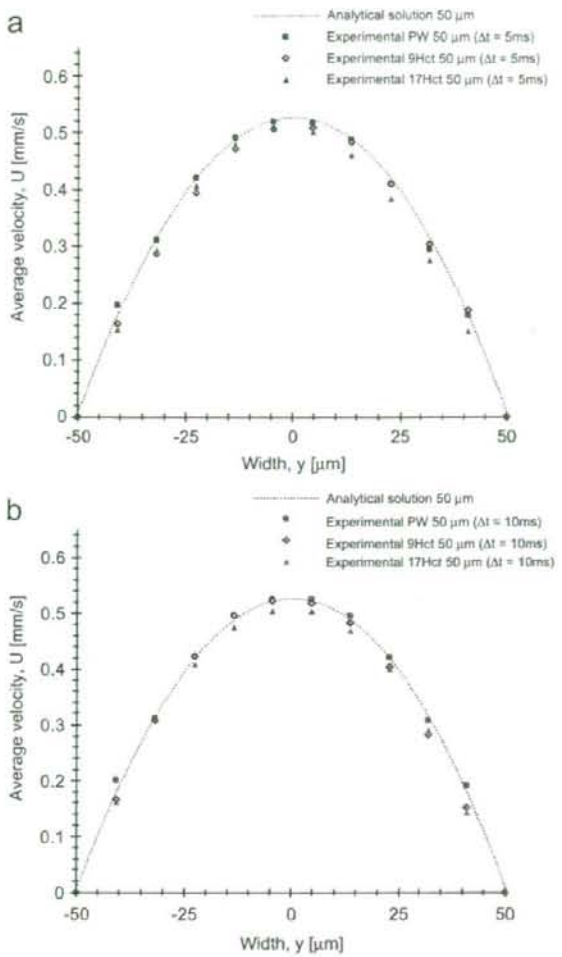

Fig. 1. Averaged ensemble velocity profiles for six different series of confocal micro-PIV measurements in the central plane (50 μm) of: (a) pure water (PW) and in vitro blood with haematocrit 9% (9 Hct) and 17% (17 Hct) for $\Delta t = 5$ ms; (b) pure water (PW) and in vitro blood (9 and 17 Hct) for $\Delta t = 10$ ms.

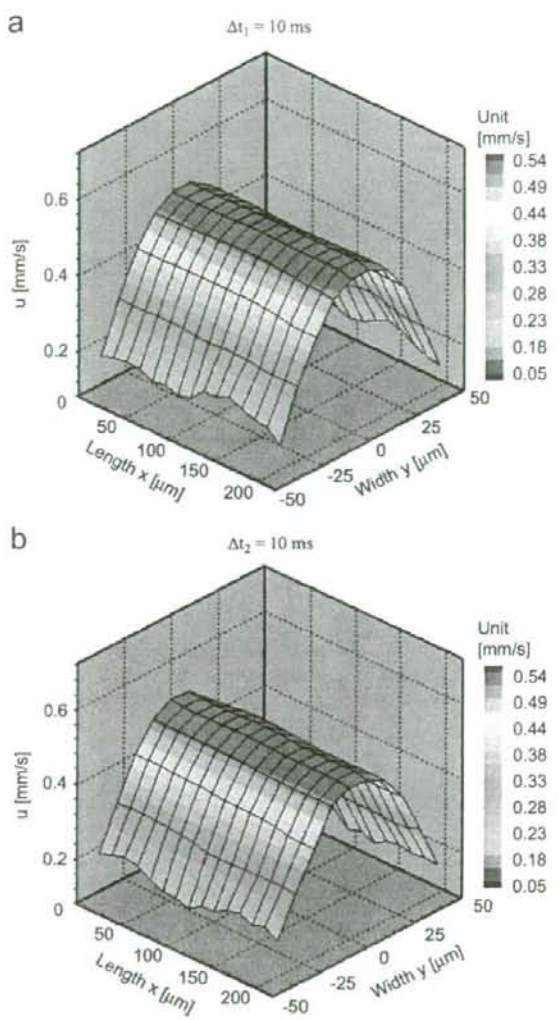

Fig. 2. Two examples showing series of instantaneous velocity profiles of pure water (PW) in the central plane (50 μm) of the microchannel for $\Delta t = 10$ ms. Note that, x, y represent, respectively, measured length and full-width of the microchannel whereas u represents the axial velocity of the working fluid along the central plane of the microchannel.

and in vitro blood with two different haematocrits at Re 0.025 for $\Delta t = 10$ ms.

In the conventional micro-PIV, most of the noise in the instantaneous velocity measurements is mainly due to the out-of-focus particle images, Brownian motion and low particle image density (Santiago et al., 1998; Nguyen and Wereley, 2002). The standard method to improve the accuracy of the conventional micro-PIV measurements is by ensembling series of instantaneous velocities. However, very recently it was shown that confocal micro-PIV, due to its optical sectioning effect provided by the spinning disk, can improve significantly the background noise even when using high particle concentration, i.e., 0.1% by volume (Park et al., 2004; Park and Kihm, 2006; Lima et al., 2006a). Furthermore, by using trace particles with 1 μm diameter it is possible to minimise some possible Brownian motion effect (Santiago et al., 1998). As a result, we believe that confocal micro-PIV can provide reliable instantaneous velocity fields, especially for homogenous fluids and in vitro blood with low haematocrit (Hct ≤ 9%) (see Appendix A).

On comparing the instantaneous velocity fields in the middle plane of pure water and in vitro blood (see Figs. 2–4), it is possible to observe that the instantaneous velocities from pure water have a nearly constant parabolic profile, whereas the instantaneous velocities from both in

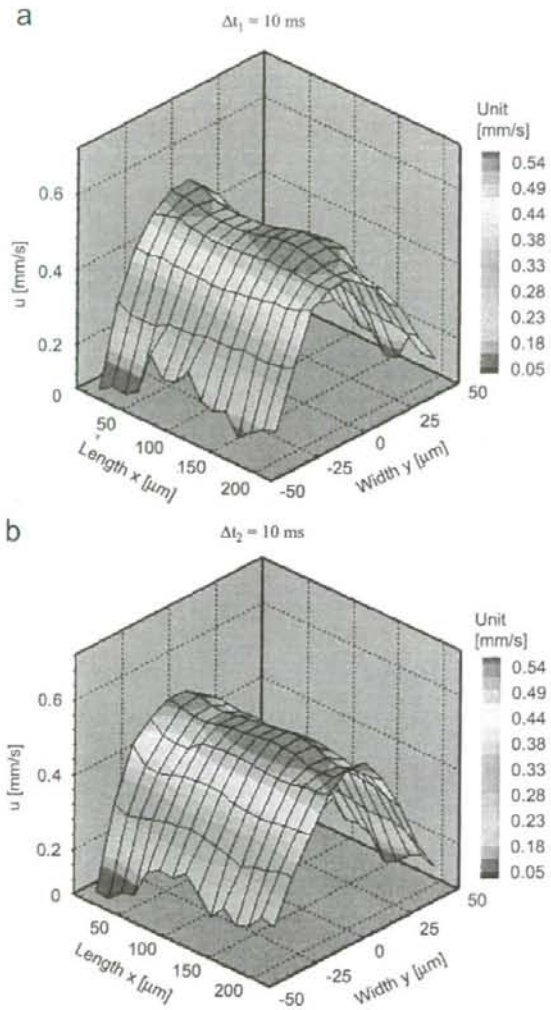

Fig. 3. Two examples showing series of instantaneous velocity profiles of in vitro blood with a 9% (9 Hct) haematocrit in the central plane of the microchannel for $\Delta t = 10$ ms.

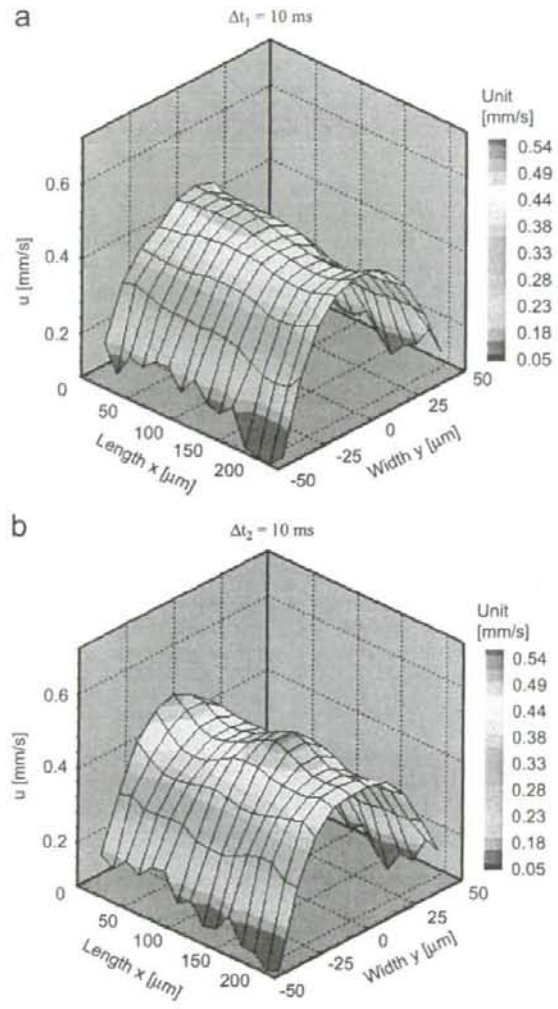

Fig. 4. Two examples showing series of instantaneous velocity profiles of in vitro blood with a 17% (17 Hct) haematocrit in the central plane of the microchannel for $\Delta t = 10$ ms.

vitro blood show some irregularities on the velocity profiles. However, these instantaneous velocity profiles are only qualitative observations which needed to be quantified in order to understand the possible causes of the fluctuations encountered on the in vitro blood instantaneous velocity profiles (see Figs. 3 and 4).

In an attempt to elucidate the possible causes of these findings we have calculated the RMS which can be determined from the ensemble averaging of the instantaneous velocity measurements. To calculate the RMS we first need to determine the standard deviation of both u and v components of the velocity at each grid point for a series of N frames using the following equations:

mean velocity components:

$$\bar{u} = \frac{1}{N}\sum_{i=1}^{N} u_i, \tag{1}$$

$$\bar{v} = \frac{1}{N}\sum_{i=1}^{N} v_i, \tag{2}$$

standard deviation of u and v components:

$$\sigma_u = \sqrt{\sum_{i=1}^{N}(u_i - \bar{u})^2/N - 1}, \tag{3}$$

$$\sigma_v = \sqrt{\sum_{i=1}^{N}(v_i - \bar{v})^2/N - 1}. \quad (4)$$

After calculating both σ_u and σ_v, RMS can be estimated by

$$\mathrm{RMS} = \sqrt{\sigma_u^2 + \sigma_v^2}. \quad (5)$$

In Fig. 5 the averaged RMS values for the three working fluids at two different Δt are plotted as a function of the microchannel width.

On comparing the RMS values with different Δt it is possible to observe that by increasing the time interval between two images the RMS decreases about 50% for PW and 9% Hct and 25% for 17% Hct. Therefore, using $\Delta t = 10$ ms the accuracy of the instantaneous velocity measurements are improved implying that the correspondent RMS values may represent a more reliable qualitative information about the time-dependent behaviour of the flow. Moreover, on comparing the RMS values from all the working fluids we have found that there is a significant difference between PW, 9 and 17% Hct at 90% confidence interval, except for some values near the wall (see Fig. 5). Despite the inclusion of some bias errors in the RMS values (see Appendix A), these results show clearly that the RMS increases with the haematocrit. We believe that the RMS values are strongly related to the fluctuations encountered in the instantaneous velocity profiles shown in Figs. 3 and 4. The reasons for these small fluctuations are still not completely clear, however, from the visualisation of the RBCs motion through the microchannel, both rotational and tumbling motion and also the interaction between the neighbouring RBCs seem to be important factors to take into account. An ongoing study to clarify the effect of the RBCs on the plasma flow is currently under way.

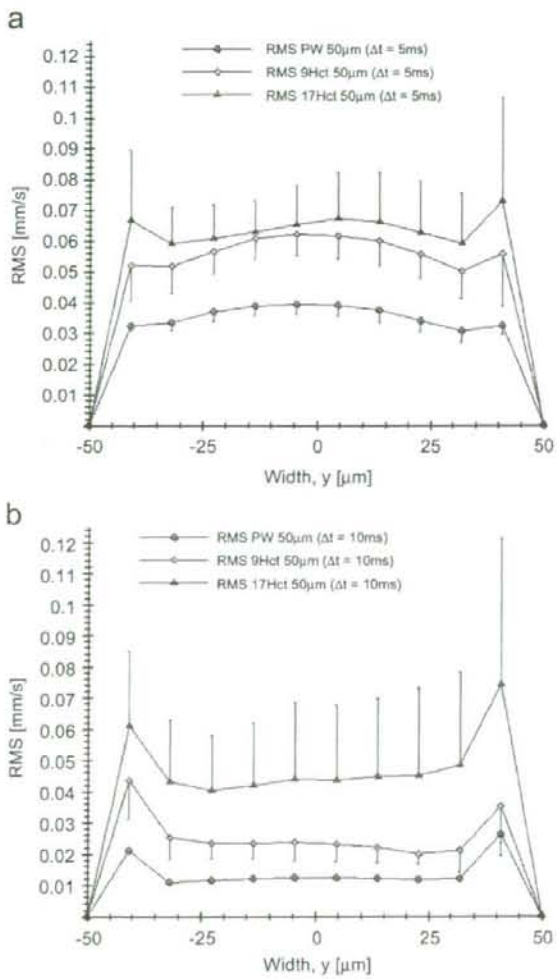

Fig. 5. Comparison of the RMS values for pure water (PW) and in vitro blood with haematocrits of 9% (9 Hct) and 17% (17 Hct) with (a) $\Delta t = 5$ ms, (b) $\Delta t = 10$ ms.

It should be noted that for haematocrits of about 17% we have observed some small random "plasma pockets" without particles in the PIV images which have created velocity vectors with small magnitudes mainly due to the light scattered and absorbed from the high concentration of RBCs within the plasma flow. Therefore, the RMS values for Hct = 17% contains quantitative information about not only the effect of the RBCs on the plasma flow but also some bias errors (see Appendix A). One way to overcome this limitation is by increasing the particles concentration within the plasma or by using a rectangular microchannel with low aspect ratio which creates an uniform distribution of RBCs (Lima et al., 2006b).

4. Conclusions

In this study, we determined both ensemble and instantaneous velocity profiles for in vitro blood (haematocrit up to 17%) flowing through a 100-μm-square microchannel. Although the ensemble velocity profiles were markedly parabolic, some fluctuations in the instantaneous velocity profiles were found to be closely related to the increase in the haematocrit. The present study shows clearly that the RMS values increase with the haematocrit implying that the presence of RBCs within the plasma flow strongly influences the measurements of the instantaneous velocity fields. The possible reasons for the RMS increase are the motion and interaction of RBCs and the light scattered and absorbed from the RBCs. This latter cause seems to be more predominant at Hct = 17%. As a result, for 17% Hct improvements on the signal-to-noise ratio are required to further enhance the measurement performance of the instantaneous velocities.

Acknowledgements

This study was supported in part by the following grants: International Doctoral Program in Engineering from the Ministry of Education, Culture, Sports, Science and Technology of Japan (MEXT), "Revolutionary Simulation Software (RSS21)" next-generation IT program of MEXT; Grants-in-Aid for Scientific Research from MEXT and JSPS Scientific Research in Priority Areas (768) "Biomechanics at Micro- and Nanoscale Levels," Scientific Research (A) no. 16200031 "Mechanism of the formation, destruction, and movement of thrombi responsible for ischemia of vital organs". The authors would like to thank Dr. Takuji Ishikawa for his valuable suggestions and discussion.

Appendix A. Supplementary data

Supplementary data associated with this article can be found, in the online version; at doi:10.1016/j.jbiomech.2007.01.012.

References

Bates, C., O'Doherty, D., Williams, D., 2001. Flow instabilities in a graft anstomosis: a study of instantaneous velocity fields. Proceedings of the Institution of Mechanical Engineers Part H 215, 579–587.

Baker, M., Wayland, H., 1974. On-line volume flow rate and velocity profile measurement for blood in microvessels. Microvascular Research 7, 131–143.

Born, G., Melling, A., Whitelaw, J., 1978. Laser Doppler microscope for blood velocity measurement. Biorheology 15, 163–172.

Bugliarello, G., Hayden, J., 1963. Detailed characteristics of the flow of blood *in vitro*. Transactions of The Society Rheology 7, 209–230.

Cochrane, T., Earnshaw, J., Love, A., 1981. Laser Doppler measurement of blood velocity in microvessels. Medical and Biological Engineering and Computing 19, 589–596.

Einav, S., Berman, R., Fuhro, P., DiGiovanni, P., Fine, S., Fridman, J., 1975. Measurement of velocity profiles of red blood cells in the microcirculation by laser Doppler anemometry (LDA). Biorheology 12, 207–210.

Gaehtgens, P., Meiselman, H., Wayland, H., 1970. Velocity profiles of human blood at normal and reduced hematocrit in glass tubes up to 130 μ diameter. Microvascular Research 2, 13–23.

Golster, H., Linden, M., Bertuglia, S., Colantuoni, A., Nilsson, G., Sjoberg, F., 1999. Red blood cell velocity and volumetric flow assessment by enhanced high-resolution laser Doppler imaging in separate vessels of hamster cheek pouch microcirculation. Microvascular research 58, 62–73.

Heise, M., Schmidt, S., Kruger, U., Ruckert, R., Rosler, S., Neuhaus, P., Settmacher, U., 2004. Flow pattern and shear stress distribution of distal end-to-side anastomoses. A comparison of instantaneous velocity fields obtained by particle image velocimetry. Journal of Biomechanics 37, 1043–1051.

Jeong, J.H., Sugii, Y., Minamiyama, M., Takeuchi, H., Okamoto, K., 2007. Interaction between liposomes and RBC in microvessels in vivo. Microvascular Research 73, 39–47.

Kinoshita, H., Oshima, M., Kaneda, S., Fujii, T., 2005. Confocal micro-PIV measurement of internal flow in a moving droplet. In: Proceedings of the Ninth International Conference on Miniaturized Systems for Chemistry and Life Sciences. Boston, MA, USA.

Lima, R., Wada, S., Tsubota, K., Yamaguchi, T., 2006a. Confocal micro-PIV measurements of three dimensional profiles of cell suspension flow in a square microchannel. Measurement Science and Technology 17, 797–808.

Lima, R., Wada, S.,Tanaka, S., Takeda, M., Tsubota, K., Ishikawa T., Yamaguchi, T., 2006b. Velocity measurements of blood flow in a rectangular PDMS microchannel assessed by confocal micro-PIV system. In: Proceedings of the World Congress on Medical Physics and Biomedical Engineering. Seoul, pp. 278–281.

Meinhart, C., Wereley, S., Santiago, J., 2000. A PIV algorithm for estimating time-averaged velocity fields. Journal of Fluids Engineering 122, 285–289.

Nakano, A., Sugii, Y., Minamiyama, M., Niimi, H., 2003. Measurement of red cell velocity in microvessels using particle image velocimetry (PIV). Clinical Hemorheology and Microcirculation 29, 445–455.

Nakano, A., Sugii, Y., Minamiyama, M., Seki, J., Niimi, H., 2005. Velocity profiles of pulsatile blood flow in arterioles with bifurcation and confluence in rat mesnetery measured by particle image velocimetry. JSME International Journal C 48 (4), 444–452.

Nguyen, N., Wereley, S., 2002. Fundamentals and Applications of Microfluidics. Artech House Inc., Norwood, MA, USA.

Park, J., Choi, C., Kihm, K., 2004. Optically sliced micro-PIV using confocal laser scanning microscopy (CLSM). Experiments in Fluids 37, 105–119.

Park, J., Kihm, K., 2006. Use of confocal laser scanning microscopy (CLSM) for depthwise resolved microscale-particle image velocimetry (μ-PIV). Optics and Lasers in Engineering 44, 208–223.

Parthasarathi, A., Japee, S., Pittman, R., 1999. Determination of red blood cell velocity by video shuttering and image analysis. Annals of Biomedical Engineering 27, 313–325.

Raffel, M., Willert, C., Kompenhans, J., 1998. Particle Image Velocimetry: A Practical Guide. Springer, Germany.

Santiago, J., Wereley, S., Meinhart, C., Beebe, D., Adrian, R., 1998. A particle image velocimetry system for microfluidics. Experiments in Fluids 25, 316–319.

Sugii, Y., Nishio, S., Okamoto, K., 2002. *In vivo* PIV measurement of red blood cell velocity field in microvessels considering mesentery motion. Physiological Measurement 23, 403–416.

Sugii, Y., Okuda, R., Okamoto, K., Madarame, H., 2005. Velocity measurement of both red blood cells and plasma of *in vitro* blood flow using high-speed micro PIV technique. Measurement Science and Technology 16, 1126–1130.

Tangelder, G., Slaaf, D., Muijtjens, M., Arts, T., Egbrink, M., Reneman, R., 1986. Velocity profiles of blood platelets and red blood cells flowing in arteriols of rabbit mesentery. Circulation Research 59, 505–514.

Tanaani, T., Otsuki, S., Tomosada, N., Kosugi, Y., Shimizu, M., Ishida, H., 2002. High-speed 1-frame/ms scanning confocal microscope with a microlens and Nipkow disks. Applied Optics 41 (22), 4704–4708.

Uijttewaal, W., Nijhof, E., Heethaar, R., 1994. Lateral migration of blood cells and microspheres in two-dimensional Poiseuille flow: a laser Doppler study. Journal of Biomechanics 27, 35–42.

Available online at www.sciencedirect.com

ScienceDirect

Colloids and Surfaces A: Physicochem. Eng. Aspects 308 (2007) 14–19

COLLOIDS AND SURFACES A

www.elsevier.com/locate/colsurfa

Preparation of multilayered silica–Gd–silica core-shell particles and their magnetic resonance images

Yoshio Kobayashi [a], Junichi Imai [b], Daisuke Nagao [b], Motohiro Takeda [c], Noriaki Ohuchi [c], Atsuo Kasuya [d], Mikio Konno [b,*]

[a] *Department of Biomolecular Functional Engineering, College of Engineering, Ibaraki University, 4-12-1 Naka-narusawa-cho, Hitachi, Ibaraki 316-8511, Japan*

[b] *Department of Chemical Engineering, Graduate School of Engineering, Tohoku University, 6-6-07 Aoba, Aramaki-aza, Aoba-ku, Sendai 980-8579, Japan*

[c] *Division of Surgical Oncology, Graduate School of Medicine, Tohoku University, Seiryo-machi, Aoba-ku, Sendai 980-8574, Japan*

[d] *Center for Interdisciplinary Research, Tohoku University, Aoba, Aramaki-aza, Aoba-ku, Sendai 980-8578, Japan*

Received 30 March 2007; received in revised form 10 May 2007; accepted 15 May 2007

Available online 18 May 2007

Abstract

A preparation method for multilayered silica–Gd–silica core-shell particles is proposed. Silica particles with an average size of 30.9 nm were prepared by the Stöber method. Silica–Gd core-shell particles with a size of 57.4 nm were synthesized by a homogeneous precipitation method at 80 °C in water/propanol solution with 27.7 M H_2O, 0.001 M $Gd(NO_3)_3$, 0.5 M urea and 1 g/l polyvinylpyrrolidone in the presence of 0.001 vol.% suspension of the silica particles. Succeeding silica-coating of the silica–Gd core-shell particles was performed with 0.0133 M TEOS and 0.002 M NaOH in the presence of a suspension of silica–Gd core-shell particles. Consequently, multilayered silica–Gd–silica core-shell particles with an average size of 71.2 nm could be obtained. These particles exhibited clear enhancement in magnetic resonance images. These nanoparticles are expected to a novel magnetic resonance contrast agents.

Keywords: Multilayer; Core-shell; Particle; Silica; Gadolinium; Stöber method; Homogeneous precipitation method; MRI

1. Introduction

Various types of core-shell nanoparticles have been emerging, and they exhibited unique properties of magnetism, electronics and optics owing to their composite structure [1–12]. We have also produced various types of silica-coated nanoparticles with seeded polymerization techniques [13–21].

Imaging by X-ray and magnetic resonance (MR) has become very important diagnostic modalities in hospitals [22,23]. Iodine compounds [22] and gadolinium compounds [24] have been used as contrast agents for X-ray CT and magnetic resonance imaging, respectively. These existing compounds may provoke adverse events as allergic reactions in patients, so that they cannot be administered to such people [22,23]. Core-shell nanoparticles are good candidates for prevention of allergic reactions because the shell materials can keep the contrast agents from living systems. We have proposed a method for silica-coating of iodine compounds as AgI nanoparticles [17], and we obtained silica-coated AgI nanoparticles that could be used as contrast agents for X-ray CT [25].

The contrast agents should be stable as colloid or dispersed in biological systems, since aggregates cause restriction of blood flow and lymph flow. Since silica particles have good stability as colloids, three layered particles with silica core, layer of contrast agent and silica shell will be more stable than contrast agents without silica core. The silica core plays a role for stability of particles and the silica shell plays a role of insulation from outside the particle.

In this study, we employed gadolinium compounds for contrast agents and fabricated multilayered silica particles with the MR contrast agent. Silica–Gd core-shell particles are prepared with a homogeneous precipitation method, and the previously performed silica-coating method is extended to the silica–Gd

* Corresponding author. Tel.: +81 22 795 7239; fax: +81 22 795 7241.
E-mail address: konno@mickey.che.tohoku.ac.jp (M. Konno).

0927-7757/$ – see front matter © 2007 Elsevier B.V. All rights reserved
doi:10.1016/j.colsurfa.2007.05.024

core-shell particles prepared. Verification of MR imaging is also performed for the multilayered particles.

2. Experimental

2.1. Materials

Tetraethylorthosilicate (TEOS) (96%), aqueous methyl amine (MA) (40% solution) and ethanol (99.5%) were used for preparation of silica cores and silica-coating as monomer, catalyst and solvent, respectively. Gadolinium nitrate hexahydrate ($Gd(NO_3)_3{\cdot}6H_2O$) (99.5%), urea (99.0%) and polyvinylpyrrolidone (PVP) (average molecular weight 36,000) were used as chemicals for Gd shell, a precipitation-inducer and a stabilizer of particles for Gd-coating, respectively. Polyvinylpyrrolidone was purchased from Nacalai Tesque Ltd. (Kyoto, Japan), and all the other chemicals were purchased from Wako Pure Chemicals Ltd (Osaka, Japan). All chemicals were used as received. Distilled and de-ionized water with an electrical resistance higher than 18 MΩ cm was used for all preparations.

2.2. Synthesis of particles

2.2.1. Silica particles

Colloidal suspensions of silica particles were prepared by a sol–gel method according to our previous paper [26]. Amine-catalytic reaction of TEOS in ethanol–water solution was carried out at initial concentrations of 0.2 M TEOS, 20 M H_2O and 0.018 M MA in a hermetically sealed flask with a magnetic stirrer. In each reaction, a solution of TEOS and ethanol was mixed with an aqueous MA solution stirring at 300 rpm and 35 °C for 24 h. Total volume of the reactant solution was about 400 ml. Colloidal suspensions of the silica particles were washed by repeating centrifugation, removal of supernatant, addition of the water and sonication over three times. Final volume of the suspension was adjusted to 20 ml with water. The silica concentration in the suspension was 0.96 vol.%, which was measured from the residue obtained after vaporization of the suspension. Fig. 1 shows TEM image of the silica particles. The silica particles were completely dispersed and had an average size of 31 ± 4 nm.

2.2.2. Silica–Gd particles

Gd-coating of the silica particles was performed by a homogeneous precipitation method in the presence of the silica particles. The Gd-coating in propanol–water solution was carried out at initial concentrations of 0.001 vol.% silica, 1 g/l PVP, 0.5 M urea and 0.001 M $Gd(NO_3)_3$ in a hermetically sealed flask reactor equipped with a mechanical stirrer. In each reaction, the silica suspension and the PVP aqueous solution were added to propanol–water solution under stirring at 300 rpm and a room temperature for 24 h. To the mixture successively added were aqueous urea solution, nitric acid (for adjusting pH to 5) and aqueous $Gd(NO_3)_3$. The mixture had a volume of about 200 ml and was stirred at 300 rpm and 80 °C for 3 h.

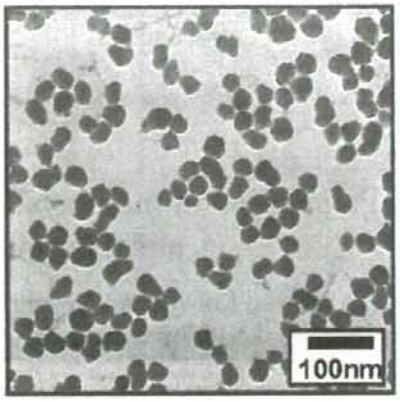

Fig. 1. TEM image of silica particles.

2.2.3. Silica–Gd–silica particles

Silica-coating of the silica–Gd core-shell particles was performed by a modified Stöber method. In each reaction, TEOS (0.59 ml) and 1.24 M aqueous NaOH solution (0.32 ml) were successively added to the suspension of silica–Gd particles (200 ml) in a hermetically sealed flask reactor equipped with a mechanical stirrer under stirring at 300 rpm and 35 °C for 24 h, which gave 0.0133 M TEOS and 0.002 M NaOH. Colloidal suspensions of silica–Gd–silica particles were washed by repeating centrifugation, removal of supernatant, addition of the water and sonication over three times.

2.3. Characterization

The particles were observed with a transmission electron microscope (TEM) (Zeiss LEO 912 OMEGA) operating at 100 kV and a scanning transmission electron microscope (STEM) (Hitachi High-Technologies HD-2000), equipped with an energy dispersive X-ray fluorescence spectrometer (EDX), operating at 200 kV. Samples for TEM and STEM were prepared by dropping and evaporating reactant mixture onto collodion-coated and uncoated copper grids, respectively. The study on the surface composition was performed using X-ray photoelectron spectroscopy (XPS). The XPS spectra were obtained by Phi 5700ci equipped with monochromatic Al Kα radiation (300 W, 14 kV, 1486.6 eV). Binding energies were calibrated relative to the C 1s peak (284.8 eV) from hydrocarbons adsorbed on the surface of the samples. To study on the composition underneath, the particle surface was etched with 2 kV Ar^+ sputtering with an etching rate of ca. 1.56 nm for one etching. ζ-Potential of particles was measured with an Ohtsuka ELS-8000 electrophretic light scattering spectrophotometer. Aqueous HCl solution or aqueous NaOH solution was added to the solution to vary pH of solution for ELS. For estimation of MR signal intensity, T1 weighted images of samples with 26 ms for the echo time and 800 ms for the repetition time were taken with a magnetic resonance imaging system (Vet-MR, ESAOTE SpA, Italy) at a static magnetic field of 0.4 T. The colloidal suspensions of particles that were washed by repeating centrifugation, removal of

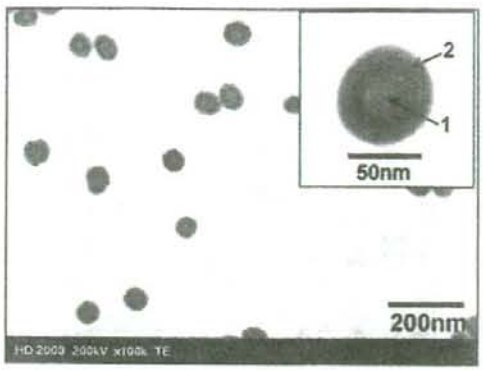

Fig. 2. STEM image of silica–Gd particles. Inset shows high-magnification image with points analyzed with EDX.

supernatant, addition of the water and sonication were used for the MR imaging.

3. Results and discussion

3.1. Silica–Gd core-shell particles

The silica–Gd particles exhibited no aggregation in the step of the Gd-coating of the silica particles, which indicated that colloidal stability of silica core particles prevented generation of aggregation. Fig. 2 shows STEM image of silica–Gd particles. The silica particles were coated with uniform shell. There was no uncoated silica particle or core-free particle. The average particle size was 57 ± 6 nm.

EDX spectra of the silica–Gd core-shell particles are shown in Fig. 3. The EDX analysis points are shown with arrows in the inset of Fig. 2. Assignments for main peaks were performed, as shown in Fig. 3. A carbon peak observed at 0.28 keV was due to contamination, and copper peaks at 8.04 and 8.90 keV were attributed to the copper grid. Peaks of SiK for 1.74 keV and GdL for 6.04 keV were used for estimation of chemical compositions. Table 1 shows results of the EDX analysis. The Gd/Si ratio of the core (point 1) and the shell (point 2) were 21.4 and 94.4 at.%, respectively. This result indicated that the shell was Gd-rich compared with the core. Accordingly, these results are the evidence that the Gd-coating of silica particles was successfully performed.

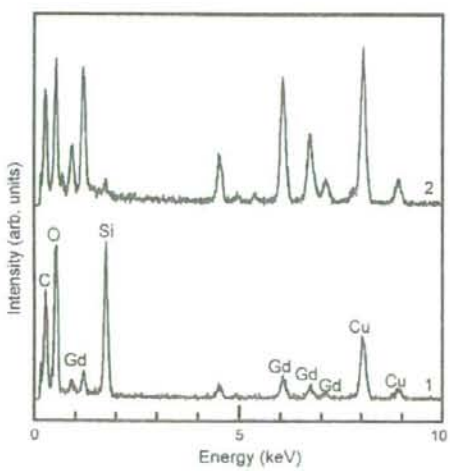

Fig. 3. EDX patterns of silica–Gd particles. Numbers 1 and 2 stand for the analysis points indicated with arrows in the inset of Fig. 2.

Table 1
EDX analysis results of silica–Gd particles

Point	Gd (at.%)	Si (at.%)
1	21.4	78.6
2	94.4	5.6

Analysis points 1 and 2 were indicated with arrows in the inset of Fig. 2.

Fig. 4 shows the Gd $3d_{5/2}$ and Si 2p spectra of the silica–Gd core-shell particles. Gadolinium $3d_{5/2}$ peak intensity for the as-prepared silica–Gd particles (number of etching: 0) was small compared to those of the etched silica–Gd particles, since the surface of silica–Gd particles might be partially covered with carbon that was probably due to contamination. As the number of etching increased, a Si 2p peak appeared and was intensified. Fig. 5 shows atomic ratios for Gd + Si estimated from XPS peak area intensity in Fig. 4. Atomic ratios of Gd and Si for the as-prepared silica–Gd particles were 93 and 7%, respectively. This result indicated that the silica core was almost covered with Gd compounds. With an increase in the number of etching, the atomic ratio of Gd decreased to ca. 80%, and the Si ratio increased to ca. 20%. This result is also an evidence for the successful Gd-coating of silica particles.

3.2. Multilayered silica–Gd–silica core-shell particles

Fig. 6 shows STEM image of multilayered silica–Gd–silica core-shell particles. Only multilayered core-shell particles were observed, and there was no core-free silica or shell-free Gd–silica particles. The silica–Gd–silica particles had an average size of 71 ± 6 nm. It was confirmed by naked eye that no sedimentation took place for the silica–Gd–silica particle colloid in 24 h after preparation. In contrast, sedimentation was observed for the silica–Gd particle colloid in 24 h after preparation. This observation indicated that the silica shell contributed to the colloidal stability.

Fig. 7 shows the EDX spectra of the silica–Gd–silica particles. Table 2 shows results of the EDX analysis that were performed for points shown with arrows in the inset of Fig. 6.

Table 2
EDX analysis results of silica–Gd–silica particles

Point	Gd (at.%)	Si (at.%)
1	17.5	82.5
2	53.4	46.6
3	22.0	88.0

Analysis points 1–3 were indicated with arrows in the inset of Fig. 4.

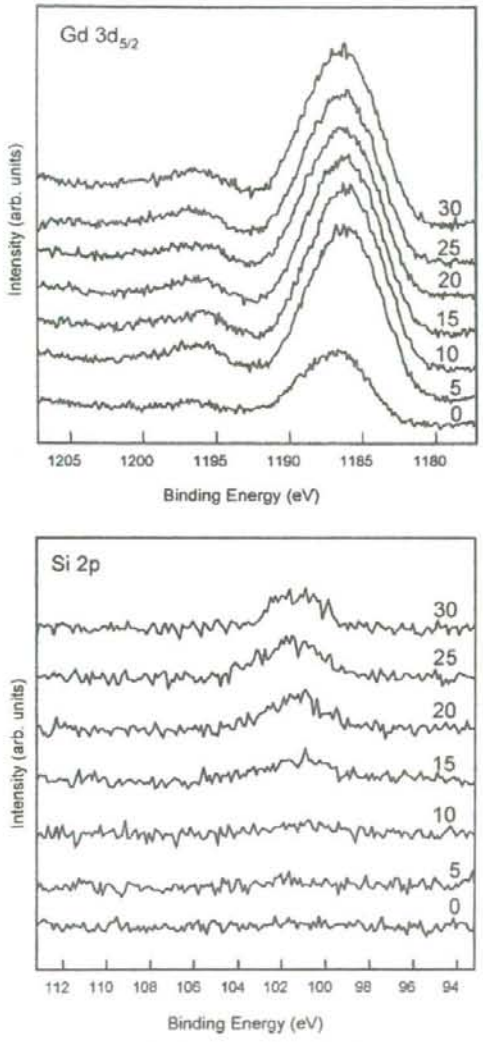

Fig. 4. XPS spectra of silica–Gd particles. Numbers 0–30 stand for number of Ar etching.

Similarly to the silica–Gd core-shell particles, the core (point 1) was Si-rich, and the inner shell on the silica core (point 2) was Gd-rich compared to the core. The Gd ratio in the outer shell on the silica–Gd core-shell particles (point 3) was 22.0 at.%, which was much lower than the inner shell. These results indicated that the silica–Gd core-shell particles were coated with silica.

Fig. 8 shows the Gd $3d_{5/2}$ and Si 2p spectra of the silica–Gd–silica particles. As the number of etching increased, an Si 2p peak intensity decreased, and in contrary, a Gd $3d_{5/2}$ peak intensity increased. Fig. 9 shows atomic ratios for Gd + Si estimated from XPS peak area intensity in Fig. 8. Atomic ratios of Gd and Si for the as-prepared silica–Gd–silica particles was almost 0 and 100%, respectively, which indicated that

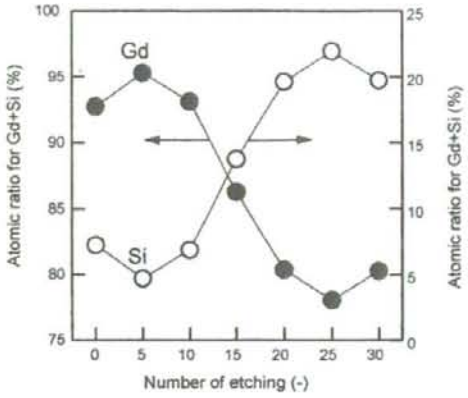

Fig. 5. Atomic ratios for Gd + Si of surface of silica–Gd particles as a function of number of Ar etching.

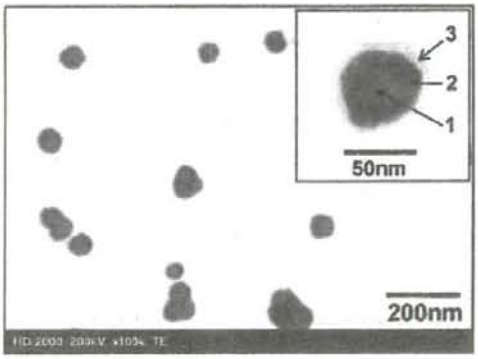

Fig. 6. STEM image of silica–Gd–silica particles. Inset shows high-magnification image with points analyzed with EDX.

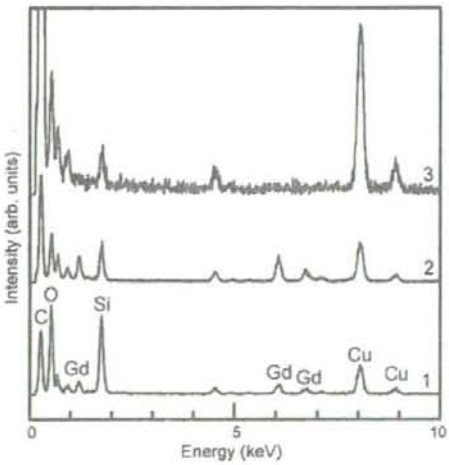

Fig. 7. EDX patterns of silica–Gd–silica particles. Numbers 1–3 stand for the analysis points indicated with arrows in the inset of Fig. 4.

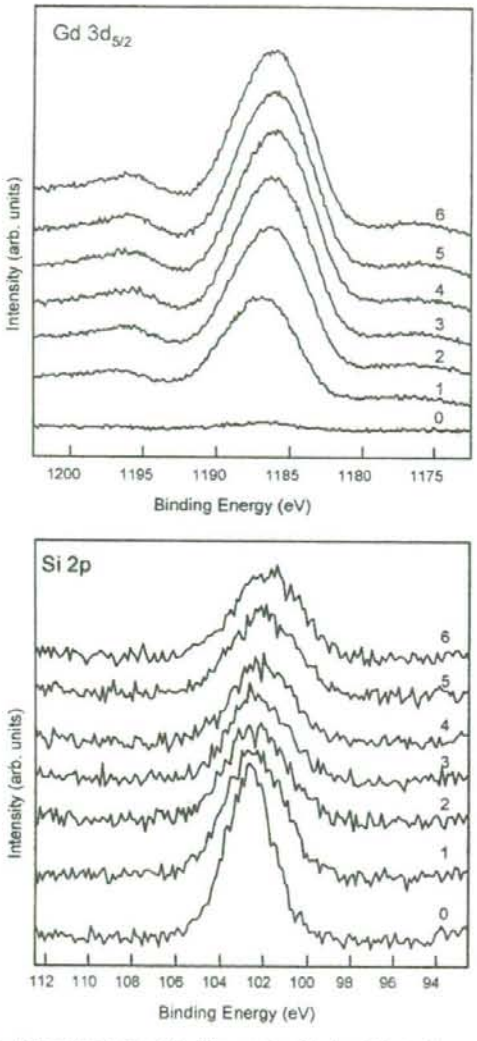

Fig. 8. XPS spectra of silica–Gd–silica particles. Numbers 0–6 stand for number of Ar etching.

the silica–Gd core was almost coated with silica. The atomic ratio of Gd increased to ca. 65%, and the Si ratio decreased to ca. 35% with the increase in the number of etching. This result indicated that the etching of outer silica shell revealed surface of silica–Gd particles, which also supported that the successful silica-coating of silica–Gd particles.

Fig. 10 shows the ζ-potentials of the silica, the silica–Gd and the silica–Gd–silica particles. Dispersion media of the as-prepared silica, silica–Gd and silica–Gd–silica particle colloids are considered to be water that contained no electrolytes, since the colloids were washed by repeating by centrifugation, removal of supernatant, addition of the water and sonication. The ζ-potentials of the as-prepared silica and the as-prepared silica–Gd particles were ca. −35 (pH 8.1) and ca. +13 mV (pH

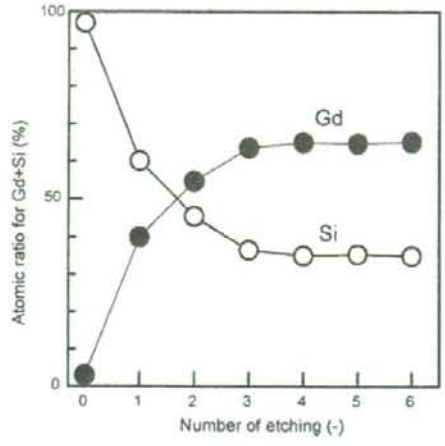

Fig. 9. Atomic ratios for Gd + Si of surface of silica–Gd–silica particles as a function of number of Ar etching.

8.0), respectively, which indicated that the silica particles were coated with Gd compounds. For the as-prepared silica–Gd–silica particles, their ζ-potential was ca. −13 mV (pH 8.0) that was between those of the silica and the silica–Gd particles. This result indicated that the surface state of the silica–Gd–silica particles was the mixture of the silica and the silica–Gd particles. Isoelectric points of the silica and the silica–Gd particles were ca. 2.5 and ca. 9.0, respectively. The isoelectric point of the silica–Gd–silica particles was ca. 2.5, which was close to that of the silica particles. These results strongly supported the results that perfect silica-coating was observed by the TEM and detected by the EDX analysis.

3.3. MRI properties

Fig. 11 shows T1 weighted images of the silica–Gd and the silica–Gd–silica particles. For comparison, MR signal intensity of water was also estimated. A faint T1 weighted image was

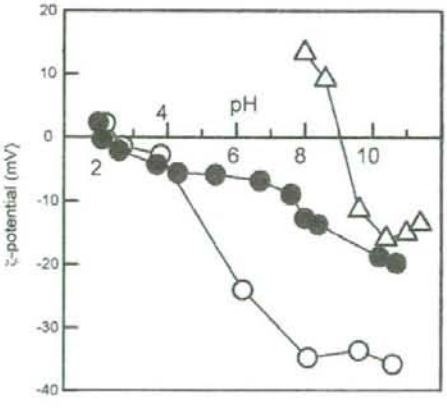

Fig. 10. ζ-Potentials of the silica (○), the silica–Gd (△), and the silica–Gd–silica particles (●).

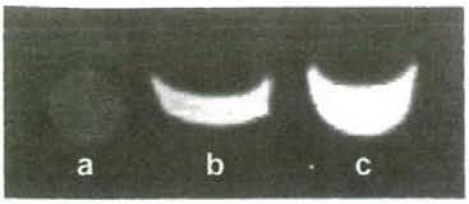

Fig. 11. T1 weighted images of (a) water, (b) silica–Gd and (c) silica–Gd–silica particles. The images were taken with 26 ms for the echo time and 800 ms for the repetition time at a static magnetic field of 0.4 T.

observed in the water. The silica–Gd and the silica–Gd–silica particles exhibited clear images. These results also support that the Gd compounds were well coated on the silica particles, and were not removed during the silica-coating.

4. Summary

A method for producing multilayered silica–Gd–silica core-shell particles has been demonstrated. Silica particles prepared through a modified Stöber method were coated with Gd compounds shells by means of a homogeneous precipitation method. Coating of silica–Gd core-shell particles with silica was achieved by a sol–gel reaction of TEOS initiated by NaOH with the aid of stabilizer PVP. The multilayered particles showed a clear contrast in magnetic resonance imaging. This property for the imaging ability is significantly useful for MRI.

Acknowledgement

This research was partially supported by the Ministry of Education of Japan, Culture, Sports, Science and Technology, a Grant-in-Aid for the COE project, Giant Molecules and Complex Systems and the Center for Interdisciplinary Research of Tohoku University.

References

[1] F. Caruso, A.S. Susha, M. Giersig, H. Möhwald, Magnetic core-shell particles: preparation of magnetite multilayers on polymer latex microspheres, Adv. Mater. 11 (1999) 950–953.
[2] F.G. Aliev, M.A. Correa-Duarte, A. Mamedov, J.W. Ostrander, M. Giersig, L.M. Liz-Marzán, N.A. Kotov, Layer-by-layer assembly of core-shell magnetite nanoparticles: effect of silica coating on interparticle interactions and magnetic properties, Adv. Mater. 11 (1999) 1006–1010.
[3] J.-I. Park, J. Cheon, Synthesis of "solid solution" and "core-shell" type cobalt-platinum magnetic nanoparticles via transmetalation reactions, J. Am. Chem. Soc. 123 (2001) 5743–5746.
[4] M. Wu, Y.D. Zhang, S. Hui, T.D. Xiao, S. Ge, W.A. Hines, J.I. Budnick, Structure and magnetic properties of SiO_2-coated Co nanoparticles, J. Appl. Phys. 92 (2002) 491–495.
[5] Y. Lu, Y. Yin, B.T. Mayers, Y. Xia, Modifying the surface properties of superparamagnetic iron oxide nanoparticles through a sol–gel approach, Nano Lett. 2 (2002) 183–186.
[6] S.M. Marinakos, D.A. Shultz, D.L. Feldheim, Gold nanoparticles as templates for the synthesis of hollow nanometer-sized conductive polymer capsules, Adv. Mater. 11 (1999) 34–37.
[7] G. Oldfield, T. Ung, P. Mulvaney, Au@SnO_2 core-shell nanocapacitors, Adv. Mater. 12 (2000) 1519–1522.
[8] L.Y. Wang, Y.-J. Lin, W.-Y. Chiu, Synthesis and properties of monodisperse conductive core-shell latexes, Synth. Met. 119 (2001) 155–156.
[9] H. Shiho, N. Kawahashi, Preparation of electrically conducting particles consisting of a polymer core and a metallic copper shell, Colloid Polym Sci. 279 (2001) 1231–1235.
[10] L.M. Liz-Marzán, M. Giersig, P. Mulvaney, Synthesis of nanosized gold-silica core-shell particles, Langmuir 12 (1996) 4329–4335.
[11] M.A. Correa-Duarte, M. Giersig, L.M. Liz-Marzán, Stabilization of CdS semiconductor nanoparticles against photodegradation by a silica coating procedure, Chem. Phys. Lett. 286 (1998) 497–501.
[12] A. Rogach, A. Susha, F. Caruso, G. Sukhorukov, A. Kornowski, S. Kershaw, H. Möhwald, A. Eychmüller, H. Weller, Nano- and microengineering: 3D colloidal photonic crystals prepared from sub-μm-sized polystyrene latex spheres pre-coated with luminescent polyelectrolyte/nanocrystal shells, Adv. Mater. 12 (2000) 333–337.
[13] Y. Kobayashi, M. Horie, M. Konno, B. Rodríguez-González, L.M. Liz-Marzán, Preparation and properties of silica-coated cobalt nanoparticles, J. Phys. Chem. B 107 (2003) 7420–7425.
[14] E. Mine, A. Yamada, Y. Kobayashi, M. Konno, L.M. Liz-Marzán, Direct coating of gold nanoparticles with silica by a seeded polymerization technique, J. Colloid Interf. Sci. 264 (2003) 385–390.
[15] Y. Kobayashi, K. Misawa, M. Kobayashi, M. Takeda, M. Konno, M. Satake, Y. Kawazoe, N. Ohuchi, A. Kasuya, Silica-coating of fluorescent polystyrene microspheres by a seeded polymerization technique and their photo-bleaching property, Colloids Surf. A 242 (2004) 47–52.
[16] S. Gu, J. Onishi, E. Mine, Y. Kobayashi, M. Konno, Preparation of multilayered gold–silica–polystyrene core-shell particles by seeded polymerization, J. Colloid Interf. Sci. 279 (2004) 284–287.
[17] Y. Kobayashi, K. Misawa, M. Takeda, M. Kobayashi, M. Satake, Y. Kawazoe, N. Ohuchi, A. Kasuya, M. Konno, Silica-coating of AgI semiconductor nanoparticles, Colloids Surf. A 251 (2004) 197–201.
[18] Y. Kobayashi, H. Katakami, E. Mine, D. Nagao, M. Konno, L.M. Liz-Marzán, Silica coating of silver nanoparticles using a modified Stöber method, J. Colloid Interf. Sci. 283 (2005) 392–396.
[19] Y. Kobayashi, K. Misawa, M. Kobayashi, M. Takeda, M. Konno, M. Satake, Y. Kawazoe, Noriaki Ohuchi, A. Kasuya, Silica-coating of fluorescent polystyrene microspheres by a modified Stöber method and their stability against photo-bleaching, e-Polymers, no. 052. 2005, pp. 1–8.
[20] E. Mine, M. Hirose, M. Kuho, Y. Kobayashi, D. Nagao, M. Konno, Synthesis of submicron-sized titania-coated silica particles with a sol-gel method and their application to colloidal photonic crystals, J. Sol-Gel Sci. Technol. 38 (2006) 91–95.
[21] Y. Kobayashi, M. Horie, D. Nagao, Y. Ando, T. Miyazaki, M. Konno, Preparation of silica-coated Co–Pt alloy nanoparticles, Mater. Lett. 60 (2006) 2046–2049.
[22] A. Joubert, M.-C. Biston, C. Boudou, J.-L. Ravanat, T. Brochard, A.-M. Charvet, F. Estève, J. Balosso, N. Foray, Irradiation in presence of iodinated contrast agent results in radiosensitization of endothelial cells: consequences for computed tomography therapy, Int. J. Radiat. Oncol. Biol. Phys. 62 (2005) 1486–1496.
[23] V. Comblin, D. Gilsoul, M. Hermann, V. Humblet, V. Jacques, M. Mesbahi, C. Sauvage, J.F. Desreux, Designing new MRI contrast agents: a coordination chemistry challenge, Coord. Chem. Rev. 185–186 (1999) 451–470.
[24] J. Feng, G. Sun, F. Pei, M. Liu, Comparison between GdDTPA and two gadolinium polyoxometalates as potential MRI contrast agents, J. Inorg. Biochem. 92 (2002) 193–199.
[25] Y. Sakurai, M. Takeda, Y. Kawazoe, A. Kasuya, Y. Kobayashi, T. Kamei, M. Nakajima, N. Ohuchi, Nanosized silver-iodide beads as new contrast media for medical application, Breast Dis. 25 (2006) 55–56.
[26] D. Nagao, E. Mine, Y. Kobayashi, M. Konno, Synthesis of silica particles in the hydrolysis of tetraethyl orthosilicate with amine catalysts, J. Chem. Eng. Jpn. 37 (2004) 905–907.

Advanced Materials Research Vols. 29-30 (2007) pp 191-194
online at http://www.scientific.net

Control of Shell Thickness in Silica-Coating of AgI Nanoparticles

Y. Kobayashi[1,2,a], K. Misawa[1,b], M. Takeda[3,c], N. Ohuchi[3,d], A. Kasuya[4,e] and M. Konno[1,f]

[1]Department of Chemical Engineering, Graduate School of Engineering, Tohoku University, Aoba, Aramaki-aza, Aoba-ku, Sendai 980-8579, Japan

[2]Department of Biomolecular Functional Engineering, Faculty of Engineering, Ibaraki University, 4-12-1 Naka-narusawa-cho, Hitachi, Ibaraki 316-8511, Japan

[3]Division of Surgical Oncology, Graduate School of Medicine, Tohoku University, Seiryo-machi, Aoba-ku, Sendai 980-8574, Japan

[4]Center for Interdisciplinary Research, Tohoku University, Aoba, Aramaki-aza, Aoba-ku, Sendai 980-8578, Japan

[a]ykoba@mx.ibaraki.ac.jp, [b]kiyoto@mickey.che.tohoku.ac.jp, [c]motot@siren.ocn.ne.jp, [d]noriakio@mail.cc.tohoku.ac.jp, [e]kasuya@cir.tohoku.ac.jp, [f]konno@mickey.che.tohoku.ac.jp

Keywords: AgI; Nanoparticle; Core-shell; Silica-coating; Sol-gel; Stöber method

Abstract. Silica-coating of AgI nanoparticles with a Stöber method was carried out to find out reaction conditions for control of the shell thickness. The AgI nanoparticles were prepared from $AgClO_4$ and KI with the use of 3-mercaptopropyltrimethoxysilane (MPS) as a silane coupling agent and dimethylamine (DMA) catalyst for alkoxide hydrolysis. The silica-coating was performed at 4.5×10^{-6}-4.5×10^{-5} M MPS, 11-20 M water, 0.002-0.1 M DMA and 0.005-0.04 M tetraethylorthosilicate at AgI concentrations of 0.1-1 mM. Consequently, AgI-silica core-shell particles could be prepared with the use of 4.5×10^{-5} M MPS, 20 M water, 0.01 M DMA and 1 mM AgI. Silica shell thickness could be varied from 15 to 28 nm with an increase in the TEOS concentration from 0.005 to 0.04 M.

Introduction

Extensive studies on silica-coated nanoparticles have been made [1-10], since the silica-coating provides a greatly enhanced colloidal stability in colloid solution. Our group also performed silica-coating of various particles such as Au [11], Ag [12] and Co [13] with sol-gel methods by applying Stöber method.

AgI has attracted much attention in the field of electronics because of its unique properties such as ionic conductivity and semiconductivity. A study on preparing AgI-silica composite particles was performed by Giersig et al. [14]. They showed that silica-coated Ag nanoparticles were mixed with I_2 solution, in which I_2 molecules diffused in silica shell layer and eventually transformed the Ag to AgI nanoparticles in the inside. However, this method with sodium silicate required long-time, and generated AgI nanoparticles on external silica surface. We have recently developed [15] a technique for silica-coating of AgI nanoparticles applying a coprecipitation from $AgClO_4$ solution and KI solution in combination with the Stöber method. In a preliminary experiment, dispersion stability of AgI nanoparticles during silica-coating was an important factor for producing AgI-silica core-shell (AgI/SiO_2) particles. Taking account of the dispersion stability of AgI nanoparticles, the present work carried out the coating experiments, in which concentrations of a silane coupling agent, water, amine catalyst, alkoxide and AgI nanoparticles were varied to find out reaction conditions suitable for the control of shell thickness.

Experimental

Chemicals. $AgClO_4$ (Kanto Chemical Co., Inc., 99 %) and KI (Wako Pure Chemicals Ltd., 99.5 %) were used as AgI precursors. Tetraethyl orthosilicate (TEOS) (Wako Pure Chemicals Ltd., 95 %), 3-mercaptopropyltrimethoxysilane (MPS) (Aldrich, 97 %) and ethanol (Wako Pure Chemicals Ltd., 99.5 %) were used for silica-coating, and dimethylamine (DMA) (Wako Pure Chemicals Ltd., 50 %) was used as a catalyst for a sol-gel reaction of TEOS and MPS. All chemicals were used as received. Ultrapure deionized water (resistivity higher than 18 MΩ cm) was used in all the preparations.

Preparation of materials. Colloids of AgI nanoparticles were prepared by mixing of $AgClO_4$ and KI solutions at a constant Ag/I molar ratio of 1/2, as follows. A freshly prepared 0.2-2 M $AgClO_4$ aqueous solution (0.015 ml) was added to 0.005-0.05 M KI aqueous solution (6 ml) under vigorous stirring at room temperature to provide AgI concentrations of 0.5×10^{-3}-5×10^{-3} M. Immediately after the mixing, color of the solution turned yellow. Particles prepared at the AgI concentration of 0.5×10^{-3} M were spherical and had an average size of 23.8 nm [20]. In their XRD pattern, peaks were observed at 22.4, 23.7, 25.4, 32.8, 39.2, 42.7 and 46.4 degree. Although these peaks were all attributable to β-AgI [16], all peaks of γ-AgI overlap with the peaks of 002 (23.7 degree), 110 (39.2 degree) and 112 (46.4 degree) of β-AgI. Accordingly, the obtained AgI nanoparticles were β-AgI or a mixture of β-AgI and γ-AgI. The Stöber method with TEOS was applied to silica-coating of the AgI nanoparticles. To the AgI colloid was added an aqueous MPS solution. After 15 min, ethanol and TEOS were successively added to the colloid. Then, the silica-coating was initiated by rapidly injecting an aqueous DMA solution into the AgI/TEOS colloid. Two series of reactions that were different in concentration conditions were examined. In *reaction A*, initial concentrations of $AgClO_4$, KI, MPS and TEOS were ranged keeping the same molar ratio of 1:2:0.045:20 at a given set of the concentrations of 11 M water and 0.01 M DMA. In *reaction B*, initial concentrations of DMA and TEOS were varied from 0.002 to 0.1 M and from 0.005 to 0.04 M, respectively, while initial concentrations of $AgClO_4$, KI and MPS were 1.0×10^{-3}, 2.0×10^{-3} and 4.5×10^{-5} M, respectively, at initial water concentration of 20 M that was high compared with the *reaction A*.

Characterization. The AgI/SiO_2 particles were characterized by transmission electron microscopy (TEM). TEM was performed with a Zeiss LEO 912 OMEGA microscope operating at 100 kV. Samples for TEM were prepared by dropping and evaporating the nanoparticle suspensions on a collodion-coated copper grid. Silica shell thickness was estimated as the difference between AgI particle and composite particle sizes.

Results and Discussion

Silica-coating in *reaction A*. Fig. 1 shows the TEM micrographs of AgI/SiO_2 particles prepared at various concentrations of $AgClO_4$, KI, TEOS and MPS in the *reaction A*. At low AgI concentrations of 0.1×10^{-3}-0.5×10^{-3} M (Figs. 1 (a)–(d)), most of the particles were quasi-perfect core-shells with AgI single core. However, at high AgI concentrations of 0.7×10^{-3} and 1×10^{-3} M (Figs. 1 (e) and (f)), particles with multiple cores were obtained. As the concentrations of $AgClO_4$, KI, TEOS and MPS rise, ionic strength of the solution should increase. Since the increase in ionic strength reduces electrostatic repulsion between the AgI nanoparticles, the reduction of electrostatic repulsion probably promoted the aggregation of AgI nanoparticles. Thus,

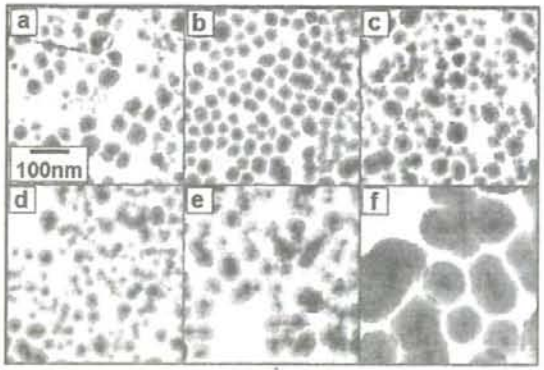

Figure 1. TEM images of AgI/SiO_2 particles. Initial concentrations of $AgClO_4$, KI, MPS and TEOS for the sample (a) were 0.1×10^{-3}, 0.2×10^{-3}, 4.5×10^{-6} and 0.002 M, respectively. For other samples, their concentrations were (b) 2, (c) 3, (d) 5, (e) 7 and 10 times higher than those of the sample (a). Initial concentrations of water and DMA were 11 and 0.01 M with respect to the total solution volume, respectively, in whole samples.

over 0.5×10^{-3} M, no AgI/SiO_2 particles that had AgI single core could be prepared with the *reaction A*.

Silica-coating in *reaction B*. To perform silica coating with the use of TEOS, ethanol is added to AgI colloid. The addition of ethanol varies dielectric constant of the colloid solution, which should affect stability of AgI nanoparticles. According to preliminary TEM observations, the AgI nanoparticles that were surface-modified with MPS were well dispersed in water, and in contrast, aggregation of the MPS-modified AgI particles took place in water/ethanol solution. MPS molecules modified AgI nanoparticle surface with their thiol groups, and consequently silanol groups were introduced onto the surface. Because the dielectric constant of water/ethanol solution is lower than water, silanol groups on the AgI particle surface probably tend to deionize in the water/ethanol solution. Thus, the electrostatic repulsion between the AgI particles was weak in the water/ethanol solution, compared with that in water. Therefore, the aggregates of AgI nanoparticles were generated in the water/ethanol solution.

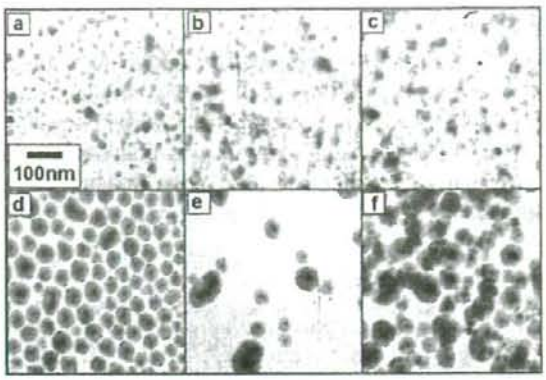

Figure 2. TEM images of AgI/SiO_2 particles prepared at DMA concentrations of (a) 0.002, (b) 0.004, (c) 0.005, (d) 0.01, (e) 0.05 and (f) 0.1 M. Initial concentrations of $AgClO_4$, KI, MPS, water and TEOS were 1.0×10^{-3}, 2.0×10^{-3}, 4.5×10^{-5}, 20 and 0.02 M with respect to the total solution volume.

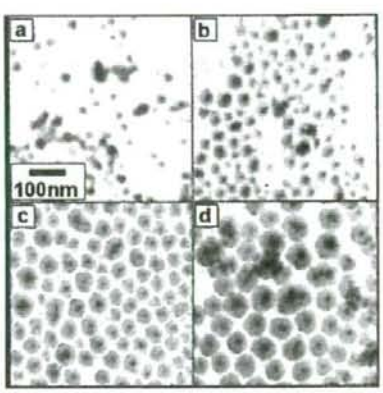

Figure 3. TEM images of AgI/SiO_2 particles prepared at TEOS concentrations of (a) 0.005, (b) 0.01, (c) 0.02 and (d) 0.04 M. Initial concentrations of $AgClO_4$, KI, MPS, DMA and water were 1.0×10^{-3}, 2.0×10^{-3}, 4.5×10^{-5}, 0.01 and 20 M with respect to the total solution volume.

According to the previous work, the AgI nanoparticles were well stabilized in water, compared with in water/ethanol solution. To improve the stability of AgI nanoparticles in sol-gel reaction, silica-coating was performed at high water concentrations. Fig. 2 shows the TEM images of AgI/SiO_2 particles prepared with the use of 20 M water at various DMA concentrations, in which an AgI concentration was 1.0×10^{-3} M. At a DMA concentration of 0.002 M, shell free AgI particles and core-free silica particles were obtained due to a shortage of DMA catalyst. At 0.004 and 0.005 M, though core-free silica particles were obtained, the AgI nanoparticles were coated with silica. At a DMA concentration as high as 0.01 M, only AgI/SiO_2 particles were observed. Addition of DMA is considered to increase the ionic strength of the solution due to the dissociation and catalyzes the hydrolysis and condensation of the alkoxysilanes [17]. Thus, the high DMA concentration should reduce the double layer repulsion between the AgI nanoparticles and the silica nuclei. As a result, the silica nuclei were efficiently deposited on the AgI particle surfaces. At DMA concentrations as high as 0.05 and 0.1 M, particles with AgI particle aggregates were observed, and the shape of the AgI/SiO_2 particles tended to be distorted. At high DMA concentrations, the AgI cores probably aggregated before becoming coated with silica due to the increased ionic strength that would promote AgI particle aggregation.

For the control of shell thickness, TEOS concentration was varied in the experiments of Figs. 3 (a)–(d). At a TEOS concentration as low as 0.005 M (Fig. 3 (a)), many core-free silica particles were generated because of low ionic strength. At TEOS concentrations of 0.01-0.04 M (Figs. 3 (b)–(d)), most of the particles were quasi-perfect core-shells with just one AgI core and the shell thickness increased from 15 to 28 nm. Thus, the TEOS concentration was found to control the silica shell thickness within a certain threshold.

Summary

AgI/SiO_2 particles were prepared by employing a sol-gel reaction of TEOS with DMA catalyst in the presence of MPS-modified AgI nanoparticles for producing AgI/SiO_2 particle colloid. The use of 4.5×10^{-5} M MPS, 20 M water, 0.01 M DMA and 1 mM AgI provided formation of AgI-silica core-shell structure. With an increase in TEOS concentration, the silica shell thickness increased from 15 to 28 nm. Concentration effects can probably be explained by the difference in ionic strength of the solution.

Acknowledgements

This research was partially supported by the Ministry of Education, Culture, Sports, Science and Technology of Japan (Grant-in-Aid for the COE project, Giant Molecules and Complex Systems), and by the Ministry of Health, Labor and Welfare of Japan.

References

[1] L. M. Liz-Marzán, M. Giersig and P. Mulvaney: Chem. Commun. (1996), p. 731

[2] S. M. Marinakos, D. A. Shultz and D. L. Feldheim: Adv. Mater. Vol. 11 (1999), p. 34

[3] V. V. Hardikar and E. Matijevic: J. Colloid Interface Sci. Vol. 221 (2000), p. 133

[4] S. R. Hall, S. A. Davis and S. Mann: Langmuir Vol. 16 (2000), p. 1454

[5] Y. Kobayashi, M. A. Correa-Duarte and L. M. Liz-Marzán: Langmuir Vol. 17 (2001), p. 6375

[6] G. Cho, B. M. Fung, D. T. Glatzhofer, J.-S. Lee and Y.-G. Shul: Langmuir Vol. 17 (2001), p. 456

[7] T. Tago, T. Hatsuta, R. Nagase, M. Kishida and K. Wakabayashi: Kagaku Kogaku Ronbunshu Vol. 27 (2001), p. 288 (in Japanese)

[8] H. Wang, H. Nakamura, Y. Yao, H. Maeda and E. Abe: Chem. Lett. Vol. 30 (2001), p. 1168

[9] Y. Lu, Y. Yin, Z.-Y. Li and Y. Xia: Nano Lett. Vol. 2 (2002) p. 785

[10] C. Graf, D. L. J.Vossen, A. Imhof and A. van Blaaderen: Langmuir Vol. 19 (2003), p. 6693

[11] E. Mine, A. Yamada, Y. Kobayashi, M. Konno and L. M. Liz-Marzán: J. Colloid Interface Sci. Vol. 264 (2003), p. 385

[12] Y. Kobayashi, H. Katakami, E. Mine, D. Nagao, M. Konno and L. M. Liz-Marzán: J. Colloid Interface Sci. Vol. 283 (2005), p. 392

[13] Y. Kobayashi, M. Horie, M. Konno, B. Rodríguez-González and L. M. Liz-Marzán: J. Phys. Chem. B Vol. 107 (2003), p. 7420

[14] M. Giersing, T. Ung, L. M. Márzan and P. Mulvaney: Adv. Mater. Vol. 9 (1997), p. 570

[15] Y. Kobayashi, K. Misawa, M. Takeda, M. Kobayashi, M. Satake, Y. Kawazoe, N. Ohuchi, A. Kasuya and M. Konno: Colloids Surfaces A Vol. 251 (2004), p. 197

[16] Y. Wang, J. Mo, W. Cai, L. Yao and L. Zhang: Mater. Lett. Vol. 56 (2002), p. 502

[17] D. Nagao, Y. Kon, T. Satoh and M. Konno: J. Chem. Eng. Japan Vol. 33 (2000), p. 468

Journal of
Nanoscience and Nanotechnology
Vol. 7, 2690–2695, 2007

Concentrated Colloids of Silica-Encapsulated Gold Nanoparticles: Colloidal Stability, Cytotoxicity, and X-ray Absorption

Yeon-Su Park[1,*], Atsuo Kasuya[1,*], Andriy Dmytruk[1], Noda Yasuto[1], Motohiro Takeda[2], Noriaki Ohuchi[3], Yoshinori Sato[4], Kazuyuki Tohji[4], Motohiro Uo[5], and Fumio Watari[5]

[1]*Center for Interdisciplinary Research, Tohoku University, Aoba-ku, Sendai 980-8578, Japan*
[2]*Department of Bioengineering and Robotics, Tohoku University, Aoba-ku, Sendai 980-8579, Japan*
[3]*Division of Surgical Oncology, Graduate School of Medicine, Tohoku University, Aoba-ku, Sendai 980-8574, Japan*
[4]*Graduate School of Environmental Studies, Tohoku University, Aoba-ku, Sendai 980-8579, Japan*
[5]*Graduate School of Dental Medicine, Hokkaido University, Kita-ku, Sapporo 060-8589, Japan*

As an effort to develop a new, effective, nontoxic X-ray contrast agent, the concentrated colloids of silica-encapsulated gold nanoparticles (Au@SiO_2 NPs) were fabricated and their colloidal stability, cytotoxicity, and X-ray absorption were investigated. The concentrated colloidal NPs were manufactured by forming a 4 nm-thick silica shell on the surface of each Au NP with 15 nm diameter, followed by enrichment to [Au] = 100 mM. They were very stable in water: the NPs were well separated each other without forming agglomerates and their optical property was very similar to that before enrichment. The colloidal stability of the NPs in biological environment was strongly dependent on their previous morphology in water. The NPs with minor shell damage were stable in phosphate buffered saline (PBS) solution: both in water and in PBS solution, they showed very similar morphology and optical property. However, the NPs with profound shell damage formed big agglomerates in PBS solution, resulting in the red-shift and broadening of the Au surface plasmon resonance peak. Cell viability and proliferation assessments revealed the biocompatibility of the Au@SiO_2 NPs: no apparent cytotoxicity was observed even at 100 ppm NPs. The concentrated colloidal NPs showed very strong X-ray absorption. Their relative X-ray transmittance to water was comparable to that of a commercial agent. Considering these, the concentrated colloids of the Au@SiO_2 NPs are suitable for an X-ray contrast agent.

Keywords: Gold, Silica, X-ray Absorption, Cytotoxicity, Colloidal Stability.

1. INTRODUCTION

As concerns on human health increase tremendously in modern society, there have been strong demands for more effective and safer medical diagnoses. One of the most indispensable modern diagnostic tools is a computed tomography (CT), which strongly relies on the contrast ability of X-ray contrast agents. Currently, tri-iodobenzene derivatives are extensively used as the contrast agents. However, sometimes these iodine-containing small organic molecules cause some serious problems such as limited imaging time, due to their short vascular circulation time, and renal toxicity. Thus, CT practices occasionally require intra-arterial catheterization which may impose serious health risks. In these regards, there have been ceaseless efforts to develop more effective and safer X-ray contrast agents.[1–5] Most of them have focused on the modification of iodine-containing contrast molecules: encapsulation in[1–4] or linkage to[5] biocompatible organic molecules/polymers. A recent report by Hainfeld et al., however, demonstrated a possibility of Au NPs for an X-ray contrast agent.[6] They obtained the contrast images of the blood vessels and some organs of mice, by utilizing concentrated colloids of 1.9 nm diameter Au NPs as an X-ray contrast agent.

The nontoxic nature of bulk Au and relatively large (e.g., a few nm or bigger in diameter) Au NPs has been well documented,[7,8] but investigations on the toxicity of small Au NPs have been scarce. Recently, Schmit et al. reported the toxicity of very small Au NPs.[9,10] The authors observed strong cytotoxicity from 1.4 nm Au NPs, of which size is in a range for deteriorative interaction with

*Authors to whom correspondence should be addressed.

1533-4880/2007/7/2690/006 doi:10.1166/jnn.2007.601

the major grooves of deoxyribonucleic acids (DNAs). Thus, for medical applications, it is highly desirable to use the Au NPs larger than DNA grooves (typically less than 2 nm). In addition to the cytotoxicity problem, the Au NPs commensurate with or smaller may cause poor X-ray contrast because of their short vascular circulation time. However, very large Au NPs are also undesirable for medical applications because of the colloidal stability of the NPs decreasing with size and the difficulty in preparing homogeneous large (e.g., 40 nm or bigger in diameter) Au NPs.[11] Taking these into account, relatively large (here, between 10 and 40 nm in diameter) Au NPs seem to be suitable for an X-ray contrast agent application.

Like many medical applications of other colloidal NPs, the application of colloidal Au NPs for an X-ray contrast agent requires them being in a highly concentrated state to ensure high X-ray contrast. However, it is not a trifle to prepare stable and concentrated colloids of relatively large Au NPs, without proper surface modifications, because of their strong tendency to coagulate in concentrated state. One of the most useful and bio-friendly surface modifications is to encapsulate each Au NP in a silica shell because silica is biocompatible, feasible for further surface modifications,[8, 12–14] and has strong negative charge in biological environment.[15] The strong negative charge on the silica surfaces, contributing to electrostatic repulsion among the NPs, may enable to prepare highly stable and concentrated colloids of relatively large Au NPs.

There has been sparse documentation[16] on the concentrated colloids of silica-encapsulated Au ($Au@SiO_2$) NPs, even though plenty of documents[12, 17–22] have been available on the morphology and optical property of the NPs and their assemblies prepared from relatively low precursor concentration without enrichment. Unfortunately, no documentation is available on the colloidal stability and cytotoxicity of $Au@SiO_2$ NPs in biological environment, which are essential factors for medical applications. Here, as an effort to develop a new class of an effective and safe X-ray contrast agent, we report the colloidal stability in biological environment, *in vitro* cytotoxicity, and X-ray absorption of the concentrated colloidal $Au@SiO_2$ NPs (Au core diameter = ca. 15 nm, silica shell thickness = ca. 4 nm), along with their morphology and optical property.

2. EXPERIMENTAL DETAILS

2.1. Materials

Hydrogen tetrachloroaurate(III) tetrahydrate ($HAuCl_4 \cdot 4H_2O$), trisodium citrate dehydrate (Na_3-Cit), formaldehyde, 0.1 M phosphate buffered saline (PBS) solution were purchased from Wako Pure Chemicals. 3-Aminopropyl trimethoxysilane (APS) was supplied by Alfa-Aesar. Sodium silicate solution (ca. 27% SiO_2), DOWEX® 50WX4-400 ion-exchange resin, alpha-Minimum Essential Medium (MEM), and fetal bovine serum (FBS) were acquired from Sigma-Aldrich. Trypan blue and alamarBlue™ were provided by Gibco and Biosource, respectively. All chemicals were used as received. Milli-Q water (>18.2 MΩ cm) was used to prepare all aqueous solutions.

2.2. Preparation

The colloids of citrate-stabilized Au NPs were prepared according to the previously reported procedure.[11, 16] Briefly, 15 ml of mildly heated 1% Na_3-Cit solution was added to 282 ml of boiling 0.532 mM $HAuCl_4 \cdot 4H_2O$ solution under stirring: the final concentrations of Au^{3+} and $citrate^-$ were 0.5 and 0.17 mM, respectively. Silica shells were formed by adding 0.75 ml of 1 mM APS solution and 12 ml of 0.54 wt% sodium silicate solution (pH = 10.5–11, adjusted by using DOWEX® 50WX4-400 ion-exchange resin) to 300 ml of the colloids of citrate-stabilized Au NPs, followed by standing the mixtures (pH ≅ 8.5) for three days.[14, 16, 17, 21] The resulting colloids of $Au@SiO_2$ NPs were cleaned by a series of washing cycle: centrifugation (25,000 × g, 15 minutes), supernatant removal, and redispersion in water. Concentrated colloids were prepared by repeating the washing cycle, while gradually decreasing the amount of water for redispersion in each cycle (hereafter, referred as a 'mild enrichment'). A typical mild enrichment consisted of 4 washing cycles. Assuming that all Au^{3+} ions were used for producing Au NPs, the concentration of metallic Au in the concentrated colloids was 100 mM, 200 times higher than that in the colloids before the enrichment. Twice repetition of the mild enrichment was also performed to investigate its influence on the morphology and optical properties of the NPs. In this case, the final concentration of metallic Au in the resulting colloidal solution was also adjusted to 100 mM. For convenience, the metallic Au concentration was used for representing the concentration of Au or $Au@SiO_2$ NPs in colloids.

2.3. Instrument and Characterization

For characterizing the morphology of the NPs, the transmission electron microscopy (TEM) was performed with a JEOL JEM-2000 microscope operating at 200 KeV. The optical property of the colloidal NPs was characterized from their visible absorption spectra obtained with a Hitach U-2000 spectrophotometer. All optical spectra were obtained after adjusting metallic Au concentration to 0.5 mM. A Rigaku Rotaflex X-ray spectrometer was used for measuring X-ray transmittances of samples.

The stability of the concentrated colloidal NPs in biological environment was characterized based on the changes in their morphology and optical property upon transferring to 0.1 M PBS solution. The volume ratio of the colloid to the PBS solution was set to 0.5.

The viability and proliferation of rat fibroblast MC3T3-E1 cells, assessed by using a almarBlue™ assay, were used for evaluating the cytotoxicity of the NPs. For cell viability tests, the rat fibroblasts were incubated at 37° in 24-well plates using alpha-MEM containing 10% FBS (10^4 cells per well) and then various amount of the NPs (0.01–100 ppm) in water were added to each well. After further incubation at 37° for 24 hours, the viability of the rat fibroblasts was estimated based on the calorimetric detection of almarBlue™ reduction caused by live cells. For cell proliferation assays, both the rat fibroblasts and the NPs in water were seeded onto 24-well plates using alpha-MEM containing 10% FBS (10^4 cells per well) and then co-incubated for 24 hours. After cell fixing with formaldehyde and staining with trypan blue, stained cells (live cells) were counted under an optical microscope. In both the tests, the control sample was rat fibroblast MC3T3-E1 cells.

3. RESULTS AND DISCUSSION

3.1. Morphology

The citrate-induced reduction of Au^{3+} produced homogeneous spherical Au NPs with ca. 15 nm in diameter (Fig. 1(a)). The $Au@SiO_2$ NPs, prepared through silica coating in the basic silicate solution, are well separated each other without forming agglomerates, as shown in Figure 1(b). They have relatively homogeneous spherical silica shells of which thickness is ca. 4 nm.

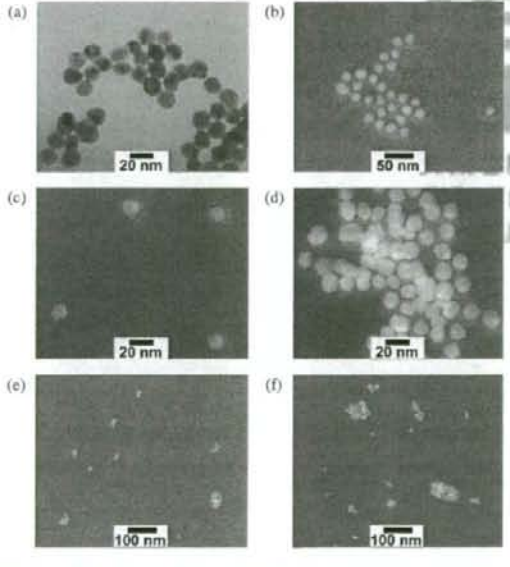

Fig. 1. TEM images of Au and $Au@SiO_2$ nanoparticles: (a) citrate-capped Au, (b) as-prepared $Au@SiO_2$ in water, (c) $Au@SiO_2$ in water after mild enrichment, (d) $Au@SiO_2$ after twice repetition of mild enrichment, (e) $Au@SiO_2$ in 0.1 M PBS solution after mild enrichment, and (f) $Au@SiO_2$ in 0.1 M PBS solution after twice repetition of mild enrichment. The concentrations of the NPs before and after the enrichments were equivalent to 0.5 and 100 mM metallic Au, respectively.

The concentrated colloidal $Au@SiO_2$ NPs, prepared through the mild enrichment, are well separated each other without forming agglomerates, even though some silica shells have minor shell damage such as detachment of some silica (Fig. 1(c)). The stability of these concentrated colloidal $Au@SiO_2$ NPs with minor shell damage (MSD) can be attributed to their high surface charge. In the experimental conditions of near neutral pH, the silica surfaces have high negative charge owing to the low isoelectric point of silica.[15] This enhances electrostatic repulsion among the NPs enough to stabilize them in the concentrated state.

The repetition of the mild enrichment exerted detrimental effect on the morphology of the $Au@SiO_2$ NPs. As shown in Figure 1(d), twice repetition of the enrichment resulted in profound shell damage (PSD): the silica shells seem to be inhomogeneous and little compact, compared with those obtained through the typical mild enrichment process; in part, they are loosely distributed among the Au NPs. Most of the NPs with PSD are poorly separated each other. In many cases, each NP is closely contacting with its immediate neighbor NPs through very thin silica barrier. Some NPs partially expose their Au cores or have big cores compose of two or more Au NPs. The formation of the big cores is related with the coagulation of the NPs with no or little silica. They have surface charge insufficient to prevent them from coagulation, because their surface charge diminishes with decreasing silica surface area.

3.2. Optical Property

As shown in Figures 2(a) and (b), the formation of 4 nm-thick silica shells caused a shift of Au surface plasmon resonance (SPR) peak from 519 to 523 nm. This red-shift by 4 nm is due to an increase in the local refractive index of the surrounding medium[17, 22] and is well in accordance with previous reports.[16, 17]

The optical property of the $Au@SiO_2$ NPs was strongly dependent on their morphology. As shown in Figure 2(c), the NPs with MSD show a SPR peak of which shape, intensity, and position are very similar to those of the NPs before the enrichment (Fig. 2(b)). The SPR peak of the NPs with PSD in Figure 2(d), however, is somewhat broad, weak, and red-shifted by 3 nm, compared with that of the NPs with MSD. These slight changes in optical property can be attributed to the close contact of the NPs and the existence of the NPs with bigger Au core.

3.3. Colloidal Stability in Biological Environment

In biological environment, the concentrated colloidal $Au@SiO_2$ NPs formed agglomerates of which size was strongly dependent on their initial morphology in water.

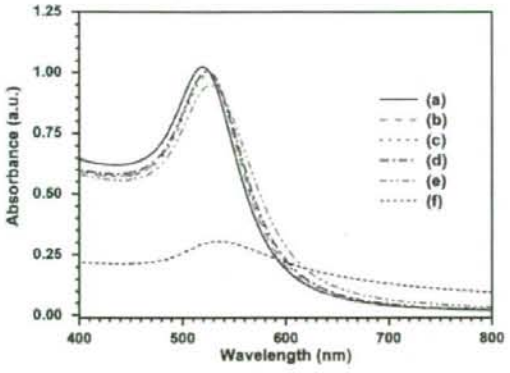

Fig. 2. Visible absorption spectra of Au and $Au@SiO_2$ nanoparticles: (a) citrate-capped Au, (b) as-prepared $Au@SiO_2$ in water, (c) $Au@SiO_2$ in water after mild enrichment, (d) $Au@SiO_2$ after twice repetition of mild enrichment, (e) $Au@SiO_2$ in 0.1 M PBS solution after mild enrichment, and (f) $Au@SiO_2$ in 0.1 M PBS solution after twice repetition of mild enrichment.

As shown in Figure 1(e), the morphology of the NPs with MSD in the PBS solution is very similar to that of the corresponding NPs in water, except for some agglomerates composed of relatively small number of the NPs. The formation of slightly more and bigger agglomerates of the NPs in the PBS solution is related with the flocculation caused by an increase in the ionic strength of the solution. Due to its high ion concentration, the PBS solution has stronger ionic strength than water. As the ionic strength of a solution increases, charge (opposite in sign) density around NPs increases. Because both ionic strength and charge density are inversely proportional to the square of the Debye shielding length, which is a measure of the strength of electrostatic potential damping from its pure value, electrostatic repulsion among the NPs is reduced and hence the NPs are destabilized with increasing ion concentration. Unlike those with MSD, the concentrated colloidal $Au@SiO_2$ NPs with PSD were unstable in the PBS solution: an immediate formation of precipitates was observed upon transferring to the solution. As shown in Figure 1(f), the TEM images of the NPs with PSD in the PBS solution show big agglomerates, along with some single NPs and small agglomerates composed of a few NPs with little or no silica shell. The big agglomerates consist of a few tens of the NPs, in which a couple of bigger Au NP cores are included. As discussed earlier, the formation of the big agglomerates of the NPs with PSD is related with the ionic strength of the PBS solution.

The optical property of the $Au@SiO_2$ NPs in PBS solution was also strongly influenced by their initial morphology: the NPs with MSD showed little change, whereas those with PSD experienced drastic change. The visible absorption spectrum of the NPs with MSD in the PBS solution (Fig. 2(e)) is very similar to that of the corresponding NPs in water (Fig. 2(c)): there is little difference in the shape, intensity, and position of the Au SPR peak. However, as shown in Figure 2(f), the NPs with PSD in the PBS solution shows a broad and weak Au SPR peak with very large background, compared with those in water (Fig. 2(d)). And their SPR peak is located at 534 nm, which is 7 nm longer than that in water. These optical observations imply the existence of various sizes of bigger NPs in the PBS solution and are well coincided with the previously described microscopic observations.

3.4. Cytotoxity

For medical applications, the $Au@SiO_2$ NPs should be biocompatible. Their biocompatibility was evaluated based on the viability and proliferation of rat fibroblast MC3T3-E1 cells. In general, 50% cell viability (or proliferation) is considered as a border of live or dead cells: materials giving 50% or higher cell viability (or proliferation) are biocompatible, while those with lower than 50% values are toxic. Figure 3 shows the viability and proliferation of the rat fibroblast cells after 24 hours incubation. In all the NP concentrations tested here, the rat fibroblast cells show more than 50% viability and proliferation. Even at a very high NP concentration of 100 ppm, the cell viability and proliferation are more than 70 and 60%, respectively. These confirm the biocompatibility of the $Au@SiO_2$ NPs. Especially the NPs show excellent biocompatibility at the concentration of 1 ppm or lower, as can be inferred from near 100% cell viability and proliferation.

3.5. X-ray Absorption

For achieving high X-ray contrast, contrast agents should show much stronger X-ray absorption (so, much lower X-ray transmittance) than human body, because X-ray contrasting ability relies on the differences in their X-ray

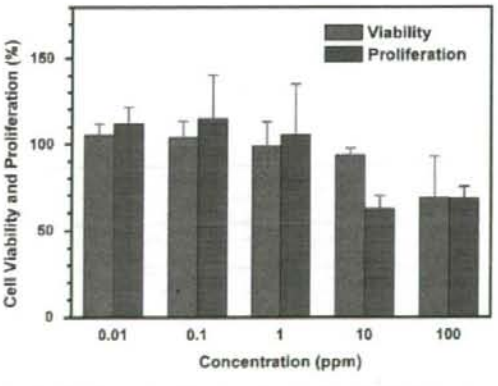

Fig. 3. Viability and proliferation of rat fibroblast MC3T3-E1 cells at various concentrations of $Au@SiO_2$ nanoparticles.

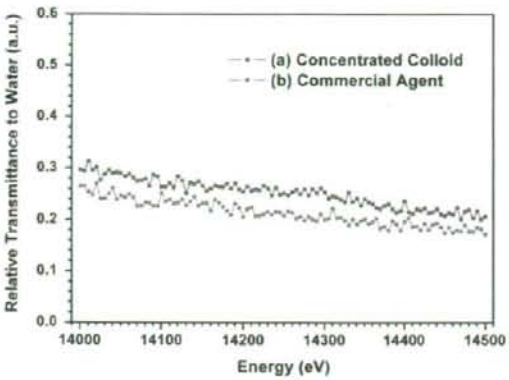

Fig. 4. Relative X-ray transmittances of (a) the concentrated colloid of $Au@SiO_2$ nanoparticles ([Au] = 100 mM) and (b) a commercial X-ray contrast agent (Iopamiron® 300). Relative transmittance = transmittance of sample/transmittance of water.

absorption. Therefore, the relative X-ray transmittance of a sample to water (a major constituent of human body) is a very important factor for evaluating its contrast ability. In general, materials with lower relative X-ray transmittance give better X-ray contrast.

Figure 4 shows the relative X-ray transmittances of the 100 mM colloidal $Au@SiO_2$ NPs and a commercial X-ray contrast agent (Iopamiron® 300). Average relative transmittance of the colloidal NPs is close to that of the commercial contrast agent. At Au L_1 edge, the colloidal NPs shows the relative transmittance of ca. 0.237, which is very close to the calculated value of 0.231 based on X-ray mass attenuation coefficient of Au. Their slight discrepancy may be mainly due to the loss of the NPs during enrichments. Considering very low relative X-ray transmittance, comparable to that of a commercial contrast agent, the concentrated colloidal $Au@SiO_2$ NPs may be suitable for an X-ray contrast agent application.

4. SUMMARY AND CONCLUSIONS

As an effort to develop a new class of an effective and nontoxic X-ray contrast agent, highly concentrated colloidal $Au@SiO_2$ NPs were prepared and their colloidal stability in biological environment, *in vitro* cytotoxicity, and X-ray absorption were investigated. Each NP consists of ca. 15 nm diameter Au core and ca. 4 nm thick silica shell. The concentration of the concentrated colloidal NPs was equivalent to 100 mM metallic Au.

Highly stable and concentrated colloidal $Au@SiO_2$ NPs with MSD were prepared through the mild enrichment. The colloidal NPs with MSD were morphologically stable in concentrated state: they were well-separated each other, without forming agglomerates. The optical property of the concentrated colloidal NPs with MSD was very similar to that of the colloidal NPs before the enrichment: there was little change in the shape, intensity, and position of Au SPR peaks before and after the enrichment.

The concentrated colloidal $Au@SiO_2$ NPs with PSD were prepared through the repetition of the mild enrichment. The concentrated colloidal NPs with PSD showed the morphology somewhat different from that of the concentrated colloidal NPs with MSD: they were poorly separated each other and had very close contact with neighbor NPs. Due to their morphology, the NPs with PSD showed a Au SPR peak which is slightly broad, weak, and red-shifted as compared with that of the NPs with MSD.

In biological environment, the stability of the concentrated colloidal $Au@SiO_2$ NPs was strongly dependent on their previous morphology in water. The concentrated colloidal NPs with MSD were stable in PBS solution, even though some small agglomerates were formed. However, the concentrated colloidal NPs with PSD were unstable in PBS solution: they formed big agglomerates, resulting in precipitation. These morphological differences affected their optical property. The colloidal NPs with MSD in PBS solution showed the Au SPR peak similar to that of the NPs in water, whereas those with PSD showed a very broad and red-shifted peak in PBS solution, as compared with those in water.

The $Au@SiO_2$ NPs are biocompatible. Both cell viability and proliferation assessments revealed no apparent cytotoxicity of the NPs even at the highest NP concentration tested here (100 ppm). Especially, at 1 ppm or lower, the NPs have an excellent biocompatibility: they showed near 100% cell viability and proliferation.

The concentrated colloidal $Au@SiO_2$ NPs showed strong X-ray absorption. Their relative transmittance to water, being inversely proportional to their X-ray contrast ability, is very low and close to that of a commercial contrast agent.

Taking into account their high colloidal stability in biological environment, excellent biocompatibility, and relative X-ray transmittance comparable to a commercial agent, the concentrated colloids of the $Au@SiO_2$ NPs, with relatively large Au core and little (or no) silica shell damage, are excellent materials for X-ray contrast agents.

Acknowledgments: This work was partially supported by Grant-in-Aid from the Ministry of Education, Science, Sports, and Culture, Japan. Authors wish to thank Prof. M. Konno of Tohoku University for his generosity in using the centrifuge.

References and Notes

1. U. P. Schmiedl, W. Krause, J. Leike, and A. Sachse, *Acad. Radiol.* 6, 164 (**1999**).
2. V. P. Torchilin, *Adv. Drug Deliv. Rev.* 54, 235 (**2002**).
3. D. R. Vera and R. F. Mattrey, *Acad. Radiol.* 9, 784 (**2002**).
4. C.-Y. Kao, E. A. Hoffman, K. G. Beck, R. V. Bellamkonda, and A. V. Annapragada, *Acad. Radiol.* 10, 475 (**2003**).
5. V. P. Torchilin, M. D. Frank-Kamenetsky, and G. L. Wolf, *Acad. Radiol.* 6, 61 (**1999**).

6. J. F. Hainfeld, D. N. Slatkin, T. M. Focella, and H. M. Smilowitz, *Br. J. Radiol.* 79, 248 (**2006**).
7. E. E. Connor, J. Mwamuka, A. Gole, C. J. Murphy, and M. D. Wyatt, *Small* 1, 325 (**2005**).
8. Z. P. Xu, Q. H. Zeng, G. Q. Lu, and A. B. Yu, *Chem. Eng. Sci.* 61, 1027 (**2006**).
9. Y. Liu, W. Meyer-Zaika, S. Franzka, G. Schmid, M. Tsili, and H. Kuhn, *Angew. Chem., Int. Ed.* 42, 2853 (**2003**).
10. M. Tsoli, H. Kuhn, W. Brandau, H. Esche, and G. Schmid, *Small* 1, 841 (**2005**).
11. G. Frens, *Nat. Phys. Sci.* 241, 20 (**1973**).
12. E. Mine, A. Yamada, Y. Kobayashi, M. Konno, and L. M. Liz-Marzán, *J. Colloid Interf. Sci.* 264, 385 (**2003**).
13. T. Schiestel, H. Brunner, and G. E. M. Tovar, *J. Nanosci. Nanotechnol.* 4, 504 (**2004**).
14. B. Rodríguez-González, A. Sánchez-Iglesias, M. Giersig, and L. M. Liz-Marzán, *Faraday Discuss.* 125, 133 (**2004**).
15. X. Cui, W.-C. Zin, W.-J. Cho, and C.-S. Ha, *Mater. Lett.* 59, 2257 (**2005**).
16. Y.-S. Park, L. M. Liz-Marzán, A. Kasuya, Y. Kobayashi, D. Nagao, M. Konno, S. Mamykin, A. Dmytruk, M. Takeda, and N. Obuchi, *J. Nanosci. Nanotechnol.* 6, 3503 (**2006**).
17. L. M. Liz-Marzán, M. Giersig, and P. Mulvaney, *Langmuir* 12, 4329 (**1996**).
18. F. Caruso, M. Spasova, V. Salgueiriño-Maceria, and L. M. Liz-Marzán, *Adv. Mater.* 13, 1090 (**2001**).
19. F. García-Santamaría, V. Salgueiriño-Maceria, C. López, and L. M. Liz-Marzán, *Langmuir* 18, 4519 (**2002**).
20. Y. Yang, M. Hori, T. Hayakawa, and M. Nogami, *Surf. Sci.* 579, 215 (**2005**).
21. I. Tunc, S. Suzer, M. A. Correa-Duarte, and L. M. Liz-Marzán, *J. Phys. Chem. B* 109, 7597 (**2005**).
22. S. Liu and M. Han, *Adv. Funct. Mater.* 15, 961 (**2005**).

Received: 25 October 2006. Revised/Accepted: 22 November 2006.